Available online at www.sciencedirect.com
ScienceDirect
Cement & Concrete Composites 29 (2007) 300–312
Cement & Concrete Composites
www.elsevier.com/locate/cemconcomp

Concrete fracture prediction using bilinear softening

Jeffrey Roesler *, Glaucio H. Paulino, Kyoungsoo Park, Cristian Gaedicke

Department of Civil and Environmental Engineering, University of Illinois at Urbana Champaign, Newmark Laboratory, 205 N. Mathews Avenue, Urbana, IL 61801-2352, USA

Received 27 April 2006; received in revised form 12 December 2006; accepted 13 December 2006
Available online 27 December 2006

Abstract

A finite element-based cohesive zone model was developed using bilinear softening to predict the monotonic load versus crack mouth opening displacement curve of geometrically similar notched concrete specimens. The softening parameters for concrete material are based on concrete fracture tests, total fracture energy (G_F), initial fracture energy (G_f), and tensile strength (f'_t), which are obtained from a three-point bending configuration. The features of the finite element model are that bulk material elements are used for the uncracked regions of the concrete, and an intrinsic-based traction-opening constitutive relationship for the cracked region. Size effect estimations were made based on the material dependent properties (G_f and f'_t) and the size dependent property (G_F). Experiments using the three-point bending configuration were completed to verify that the model predicts the peak load and softening behavior of concrete for multiple specimen depths. The fracture parameters, based on the size effect method or the two-parameter fracture model, were found to adequately characterize the bilinear softening model.

Keywords: Concrete; Cohesive zone model; Fracture energy; Size effect; Two-parameter fracture model

1. Introduction

Concrete is a quasi-brittle material, which means its fracture process zone size is not small compared with the typical specimen or structural dimension. Classical linear elastic fracture mechanics (LEFM) is unable to predict the progressive failure of concrete specimens due to this large nonlinear process zone [1]. In order to overcome LEFM limitations for concrete, Hillerborg et al. [2] extended the cohesive crack model, developed by Barenblatt [3] and Dugdale [4], to predict concrete fracture with the finite element method. Based on the cohesive crack model, Hillerborg et al. [2], Modeer [5], Petersson [6], Roelfestra and Wittmann [7] and Mulule and Dempsey [8] predicted fracture behavior of quasi-brittle materials with the fictitious crack model which requires a pre-existing crack [9]. To extend to notchless specimens for other types of materials, the cohesive zone model (CZM) has been widely used to predict crack propagation through numerical simulation [10–13]. The majority of cohesive zone models are based on intrinsic formulations which require a pre-defined crack path and a penalty stiffness prior to the softening behavior, as shown in Fig. 1a. Bulk material elements are used for the uncracked regions, and cohesive elements with an intrinsic-based traction-opening constitutive relationship are employed along the expected fracture surface.

The intrinsic CZM has of four stages as shown in Fig. 1b. The first stage is characterized by general elastic material behavior without separation (Fig. 1b: Stage I). The concrete material properties are assumed to be homogeneous and linear elastic in this stage. The next stage is the initiation of a crack when a certain criterion is met, for example, critical tensile bending stress (Fig. 1b: Stage II). In this study, the fracture initiation criterion for mode I fracture is assumed to occur when the state of stress reaches the cohesive strength (e.g. concrete tensile strength, f'_t). Stage III describes the evolution of the failure, which is

* Corresponding author. Tel.: +1 217 265 0218; fax: +1 217 333 1924.
E-mail address: jroesler@uiuc.edu (J. Roesler).

0958-9465/$ - see front matter © 2007 Elsevier Ltd. All rights reserved.
doi:10.1016/j.cemconcomp.2006.12.002

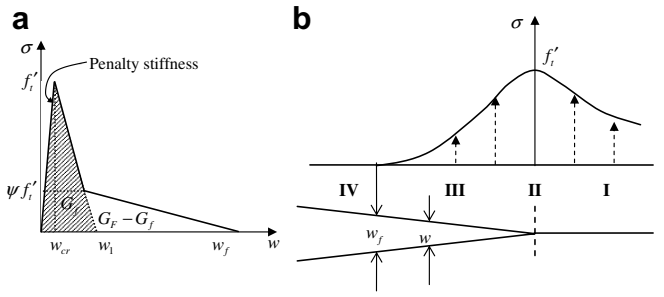

Fig. 1. (a) Bilinear softening for concrete and (b) four stages of the cohesive zone model.

governed by the cohesive law or the softening curve, i.e., the relation between the stress ($\boldsymbol{\sigma}$) and crack opening width (w) across the fracture surface, as shown in Fig. 1b (Stage III). Because the cohesive law defines the characteristic of the fracture process zone, the shape of the softening curve in the CZM is essential for predicting the fracture behavior of the structure. The final stage defines local failure when the crack opening width reaches the final crack opening width (w_f) (Fig. 1b: Stage IV). In this stage, concrete surfaces created by the fracture process have no traction (no load bearing capacity).

Different constitutive relationships, such as a linear [2], bilinear [6,7,14], trilinear [15], and exponential [16] softening curve, have been developed to predict the fracture behavior of concrete materials. Among the various softening curves, the bilinear softening relationship has been used extensively and is the model of choice in this work. Petersson [6] originally proposed a bilinear softening curve with a fixed kink point, which was also adopted by Gustafsson and Hillerborg [17]. Wittmann et al. [18] determined a bilinear softening curve with the stress ratio of the kink point at 0.25. Elices et al. [12] and Guinea et al. [19] characterized a bilinear softening curve using the tensile strength, the total fracture energy, and two parameters which represent the shape of a softening curve. Bazant [20] further refined the bilinear softening model by introducing an additional fracture parameter called the initial fracture energy. In this research, the bilinear softening model offered by Bazant [21] was selected since the softening curve has two slopes which can be controlled by the measured concrete fracture properties.

The key contribution of this paper is directly linking the experimental fracture properties with the bilinear softening curve and implementation into a finite element-based CZM in order to predict the concrete specimen fracture behavior including the size effect. Due to the relationship between the experimental fracture properties and the bilinear softening curve, shown in Fig. 1a, no additional fitting to the softening curve is required to match the three-point bending (TPB) test experimental data. The following experimental concrete fracture parameters that define the bilinear softening curve shape are simple to measure using TPB and split tensile testing configuration: total fracture energy (G_F), initial fracture energy (G_f), and tensile strength (f_t'). The CZM allows for size effect predictions based on the concrete material dependent properties (G_f and f_t') and the size dependent property (G_F). Based on the experimentally-defined bilinear softening curve, the finite element-based CZM was developed to predict the monotonic load versus crack mouth opening displacement (CMOD) with different specimen sizes.

2. Implementation of the cohesive zone model for concrete

The cohesive element is formulated exploiting the principle of virtual work. The internal work done by the virtual strain ($\delta\boldsymbol{\varepsilon}$) in the domain ($\Omega$) and the internal work done by the virtual crack opening displacement ($\delta\mathbf{w}$) along the crack line (Γ_c), is equal to the external work done by the virtual displacement ($\delta\mathbf{u}$) at the traction boundary (Γ):

$$\int_{\Omega} \delta\boldsymbol{\varepsilon}^{\mathrm{T}}\boldsymbol{\sigma}\,\mathrm{d}\Omega + \int_{\Gamma_c} \delta\mathbf{w}^{\mathrm{T}}\mathbf{T}\,\mathrm{d}\Gamma_c = \int_{\Gamma} \delta\mathbf{u}^{\mathrm{T}}\mathbf{P}\,\mathrm{d}\Gamma, \tag{1}$$

where $\mathbf{T}$ is the traction vector along the cohesive zone, and $\mathbf{P}$ is the external traction vector. The first term in Eq. (1) is the internal virtual work of the bulk element, while the second term in the equation denotes the internal virtual work of the cohesive element. The right hand side of Eq. (1) represents the external virtual work. By using the derivative of the shape function matrix ($\mathbf{B}$) and interpolating the crack opening displacement into the nodal displacement through the shape function matrix ($\mathbf{N}$), the following formulation can be obtained:

$$\left[\int_{\Omega} \mathbf{B}^{\mathrm{T}}\mathbf{D}\mathbf{B}\,\mathrm{d}\Omega + \int_{\Gamma_c} \mathbf{N}^{\mathrm{T}}\frac{\partial\mathbf{T}}{\partial\mathbf{w}}\mathbf{N}\,\mathrm{d}\Gamma_c\right]\mathbf{u} = \int_{\Gamma} \mathbf{P}\,\mathrm{d}\Gamma, \tag{2}$$

where $\mathbf{D}$ is the material tangential matrix for the bulk element. The stiffness matrix and load vector of the cohesive element are assembled as a user-defined subroutine [22].

2.1. Numerical implementation

In order to satisfy the different variables of the stress function, two different elements are used in cohesive zone modeling. One is the general linear elastic element, called the bulk element, which has the following stress and strain relationship

$$\boldsymbol{\sigma}_{\text{bulk element}} = f_{\text{elastic}}(\boldsymbol{\varepsilon}). \tag{3}$$

The bulk element employs two-dimensional plane stress assumptions to represent the linear elastic behavior (f_{elastic}) in stage I. The other element is the cohesive surface element, which has the following traction and separation relationship:

$$\boldsymbol{\sigma}_{\text{cohesive element}} = f_{\text{cohesive law}}(\mathbf{w}). \tag{4}$$

The cohesive element contains the features ($f_{\text{cohesive law}}$) of the crack initiation criterion (stage II), the nonlinear cohesive law (stage III) and the failure condition (stage IV). The discrete cohesive element is distinct from continuum-based strain softening elements [33]. The cohesive surface element

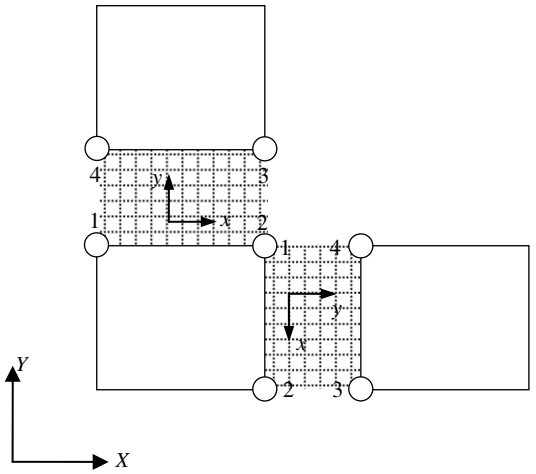

Fig. 2. Coordinate system and element nodal numbering in the cohesive surface element.

is implemented in ABAQUS as a user element (UEL) subroutine. As a result, inserting the cohesive surfaces between bulk elements bridges the continuum (e.g. linear elastic) and fracture behavior of the material [10,23–25]. The complete UEL subroutine for ABAQUS is provided in Ref. [24].

In the numerical simulation, the rectangular plane stress element (Q4) is used for bulk element, while the cohesive surface element is inserted along the crack path. Fig. 2 is a general illustration of the cohesive zone element. Fig. 3 illustrates the finite element mesh for specimen size $D = 63$ mm and the cohesive surface element inserted along the crack path prior to the numerical simulation (preprocessing). This research is concerned with mode I fracture. Therefore, the crack is assumed to propagate on a straight line in the vertical direction. For an arbitrary crack propagation using the intrinsic CZM see Song et al. [25]. Based on a parametric study [13], the size of the cohesive element was selected to be 1 mm which is small enough to capture the local fracture process.

2.2. Determination of the softening curve

To characterize the CZM, it is essential to determine the shape of the softening curve. The bilinear softening curve (Fig. 1a) is adopted in order to define the fracture initiation at the cohesive strength, to capture the maximum load of the specimen, and to describe the post-peak behavior. The fracture initiation condition (f'_t), is obtained by introducing the penalty stiffness (f'_t/w_{cr}). When a crack opening width reaches a critical crack opening width (w_{cr}), the traction corresponds to the maximum tensile strength

$$f'_t = f_{\text{cohesive law}}(w_{cr}). \tag{5}$$

The initial slope of the softening curve is derived from the initial fracture energy measured by the size effect method (SEM) or by the two-parameter fracture model (TPFM), and represents the peak load of the specimen. Finally, the tail of the softening curve characterizes the post-peak load behavior, which is related to the difference between the total fracture energy (G_F) and the initial fracture energy (G_f).

In order to specify the coordinates of the intrinsic bilinear softening curve, four unknown constants and the penalty stiffness are needed as shown in Fig. 1a: f'_t, w_1, w_f, ψ and w_{cr}. Since the initial penalty stiffness is determined based on the numerical stability conditions associated with a user-defined subroutine (e.g. UEL in ABAQUS), the ratio of f'_t/w_{cr} is fixed, and therefore only four parameters are required. In this study, three unknown constants (f'_t, w_1 and w_f) are obtained by the three experimental fracture parameters: the initial fracture energy (G_f), the total fracture energy (G_F) and the concrete tensile strength (f'_t) following a procedure published by Bazant [21]. The other parameter, the ratio (ψ) of the cohesive stress and f'_t at the kink point, is generally between 0.15 and 0.33 [20]. The initial fracture energy is defined as the area under the first and second slope of the curve in Fig. 1a. This is because the initial fracture energy controls the maximum loads of structures and thus the size effect [20], as noted

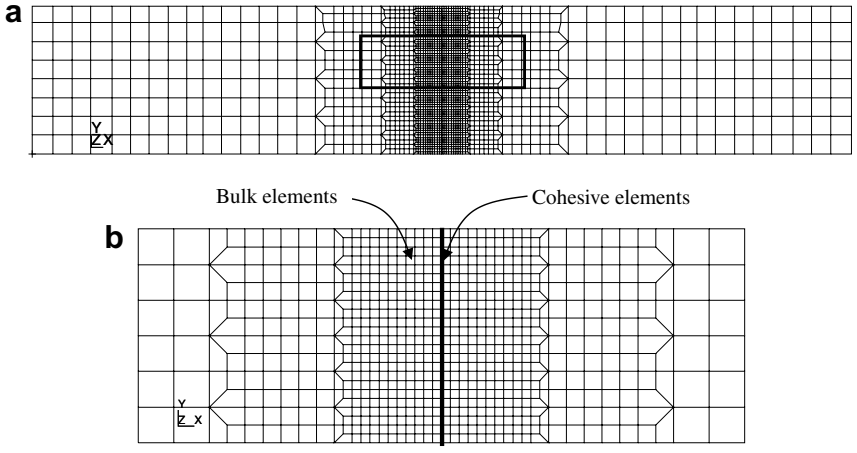

Fig. 3. (a) Finite element mesh for specimen size $D = 63$ mm and (b) zoom of mesh along the cohesive element region.

by Planas et al. [26]. Therefore, the horizontal axis intercept of the initial descending curve is defined as

$$w_1 = \frac{2G_f}{f'_t}. \quad (6)$$

Similarly, the horizontal axis intercept of the tail of the softening curve is defined as the final crack opening width:

$$w_f = \frac{2}{\psi f'_t}[G_F - (1-\psi)G_f]. \quad (7)$$

This expression is obtained by equating the total fracture energy with the area under the bilinear softening curve.

3. Experimental design and concrete material properties

An experimental program was designed to develop and verify the proposed CZM for concrete monotonic fracture. Table 1 lists the type, identification and dimensions of each beam tested in this research. Each beam was identified using the letters "B" or "CB", for cast and cut beams, respectively, followed by the depth, the width and finally a letter to individualize each specimen (a, b or c). The TPB test configuration is shown in Fig. 4. Three sizes of notched beams were cast with the following depths (D): 250, 150, 63 mm. Three concrete specimens were cast for each size. All notches were cast into the specimen. Additionally, three 63 mm depth (D) beams were cut from the larger beams after failure, to compare them with the cast beams. These beams were needed due to the large variability in the results for the 63 mm specimens. The CB specimens also had saw-cut notches instead of cast notches. All specimens had a thickness of 80 mm, a notch to depth ratio (a_0/D) of 1/3 and were tested with a span to depth (S/D) ratio of 4, as shown in Fig. 4.

Table 1
Three-point bending test specimens

Beam type	Specimen ID	Specimen dimensions (mm)				
		Length (L)	Depth (D)	Thickness (t)	Notch (a_0)	Span (S)
Cast	B250-80a	1100	250	80	83	1000
	B250-80b	1100	250	80	83	1000
	B250-80c	1100	250	80	83	1000
	B150-80a	700	150	80	50	600
	B150-80b	700	150	80	50	600
	B150-80c	700	150	80	50	600
	B63-80a	350	63	80	21	250
	B63-80b	350	63	80	21	250
	B63-80c	350	63	80	21	250
Cut	CB63-80a	350	63	80	21	250
	CB63-80b	350	63	80	21	250
	CB63-80c	350	63	80	21	250

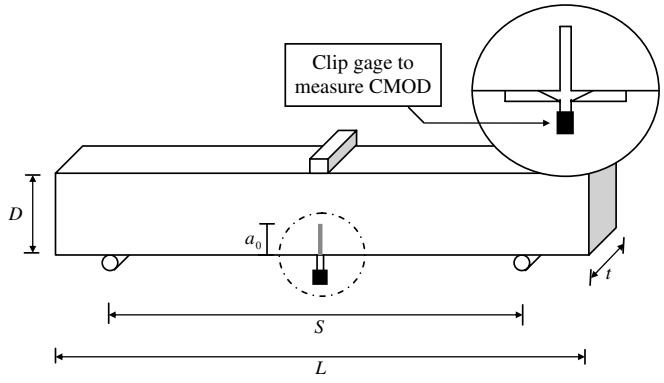

Fig. 4. Specimen dimensions and test configuration ($S/D = 4$).

3.1. Concrete materials and mix design

In order to validate the CZM, a single concrete mix design was used as shown in Table 2. This mix contained a limestone coarse aggregate with a maximum size of 19 mm, and manufactured sand. A water to cementitious ratio of 0.42 was used with a 23% replacement of Type I cement with Type C fly ash. The mixture also contained a water reducer (Type D), an air entrainment agent, and a high range water reducer (Type F).

3.2. Fresh and hardened concrete properties

The density, slump and air content are presented in Table 3. Nine 150 mm by 300 mm cylinders were cast to obtain the compressive strength, split tensile strength,

Table 2
Concrete constituent classification and mix proportions

Material	Specification	Quantity
Coarse aggregate	ASTM C33, crushed limestone # 67	1107 kg/m^3
Fine aggregate	ASTM C33	718 kg/m^3
Cement	ASTM C150, Type I	290 kg/m^3
Fly ash	ASTM C618, Type C	88 kg/m^3
Water	N/A	160 lt/m^3
Air entrainment admixture	ASTM C260	0.24 lt/m^3
Water reducer	ASTM C494 Type D	1.68 lt/m^3
High range water reducer	ASTM C494 Type F	1.65 lt/m^3

Table 3
Average fresh and hardened properties of the concrete

Property	Specification	Quantity
Fresh concrete		
Density	ASTM C138	2403 kg/m^3
Lump	ASTM C143	100 mm
Air content	ASTM C231	2.8%
Hardened concrete		
Compressive strength	ASTM C39	58.3 MPa
Split strength	ASTM C496	4.15 MPa
Modulus of elasticity	ASTM C469	32.0 GPa

and modulus of elasticity. All beam and cylinder specimens were demolded after 24 ± 2 h, and then covered with wet burlap for 7 days. After that period, all specimens were stored in a room with temperatures ranging from 20 to 25 °C, until they were tested at 119 days. Table 3 also illustrates the hardened concrete properties, which were an average compressive strength of 58.3 MPa, split tensile strength of 4.15 MPa, and modulus of elasticity of 32.0 GPa.

3.3. Testing protocol of three-point bending experiments

The loading rate of the specimens was controlled by the CMOD gage. The rate of the CMOD displacement control was 0.001 mm/s until the beam reached its peak load and then it was unloaded in 15 s. The loading and unloading procedure enabled construction of loading and unloading compliance curves and creation of the overall failure envelope, as shown in Fig. 5. Twenty load and unload cycles

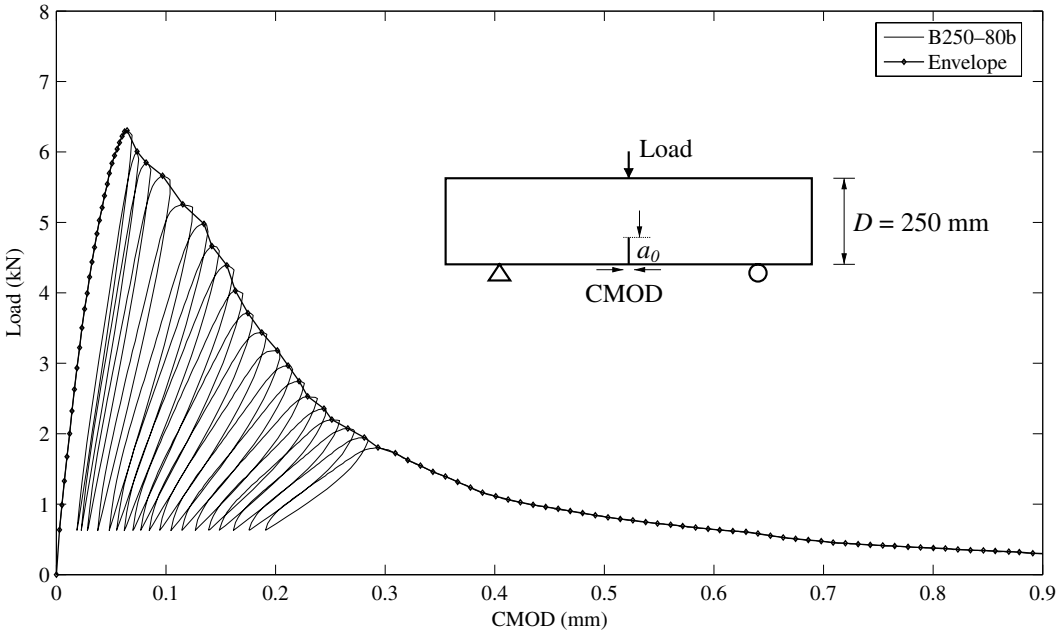

Fig. 5. Load–CMOD cycles and envelope curve for B250-80b specimen.

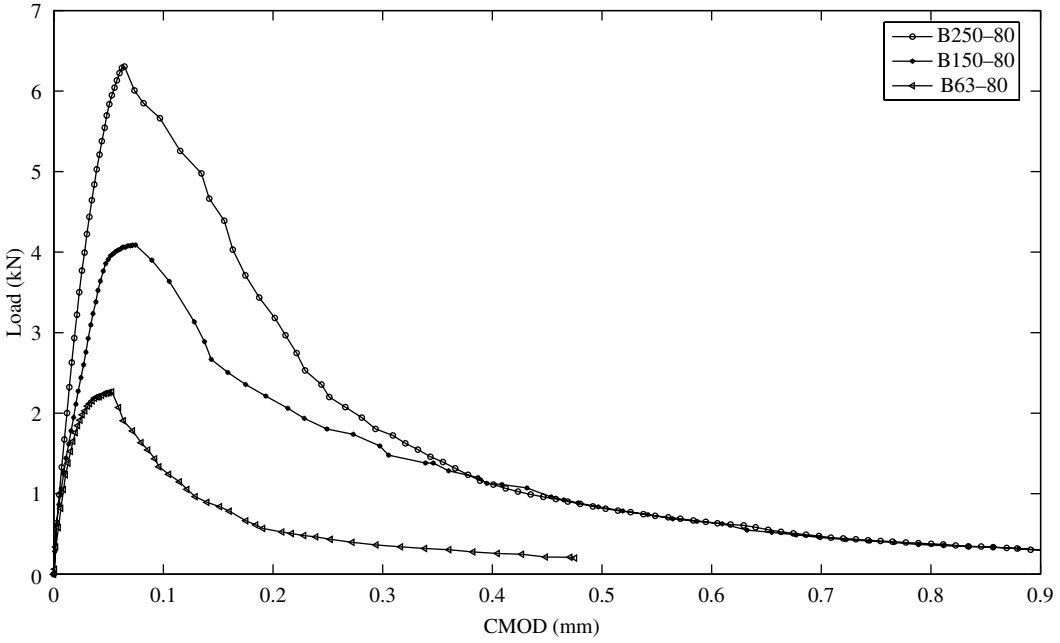

Fig. 6. Average envelope curves for each specimen size (63, 150, and 250 mm).

were produced for each specimen with the final cycle loading the beam until complete fracture.

4. Test results and calculation of fracture parameters

From the experimental beam fracture data, the following fracture quantities were calculated and summarized: total fracture energy (G_F), the critical stress intensity factor (K_{IC}), critical crack tip opening displacement ($CTOD_C$), initial fracture energy (G_f), and the characteristic length of the fracture process zone (c_f).

4.1. Total fracture energy (G_F)

Fig. 6 shows the average load–CMOD envelope curve for each of the three specimen depths. The total fracture energy (G_F) or specific fracture energy is based on Hillerborg's work-of-fracture method [27], which is defined as the ratio between the total energy (W_t), and the area of concrete fracture, $(D - a_0)t$. The total energy (W_t) is calculated as the summation of the area (W_0) under the raw load (P_a) versus CMOD curve and $P_w\delta_0$, where P_a is the raw load applied by the testing machine (without considering

Table 4
Three-point bending test results

Beam type	Specimen ID	Test results							
		Peak load (kN)	Total fracture energy		TPFM			SEM	
			G_F (N/m)	CV (%)	K_{IC} (MPa m$^{1/2}$)	CV (%)	$CTOD_C$ (mm)	G_f (N/m)	c_f (mm)
Cast	B250-80a	6.926	193	16.2	1.261	11.8	0.0167	52.1	24.36
	B250-80b	6.303	139		1.203		0.0181		
	B250-80c	6.866	169		1.497		0.0319		
	B150-80a	N/A	N/A	4.7	N/A	7.1	N/A		
	B150-80b	4.089	170		1.086		0.0255		
	B150-80c	4.158	159		0.983		0.0115		
	B63-80a	N/A	N/A	N/A	N/A	14	N/A		
	B63-80b	2.264	106		1.012		0.0159		
	B63-80c	2.054	N/A		0.834		0.0115		
Cut	CB63-80a	2.725	123	0.3	1.130	13	0.0142		
	CB63-80b	2.749	124		1.002		0.0075		
	CB63-80c	2.820	123		1.293		0.0184		

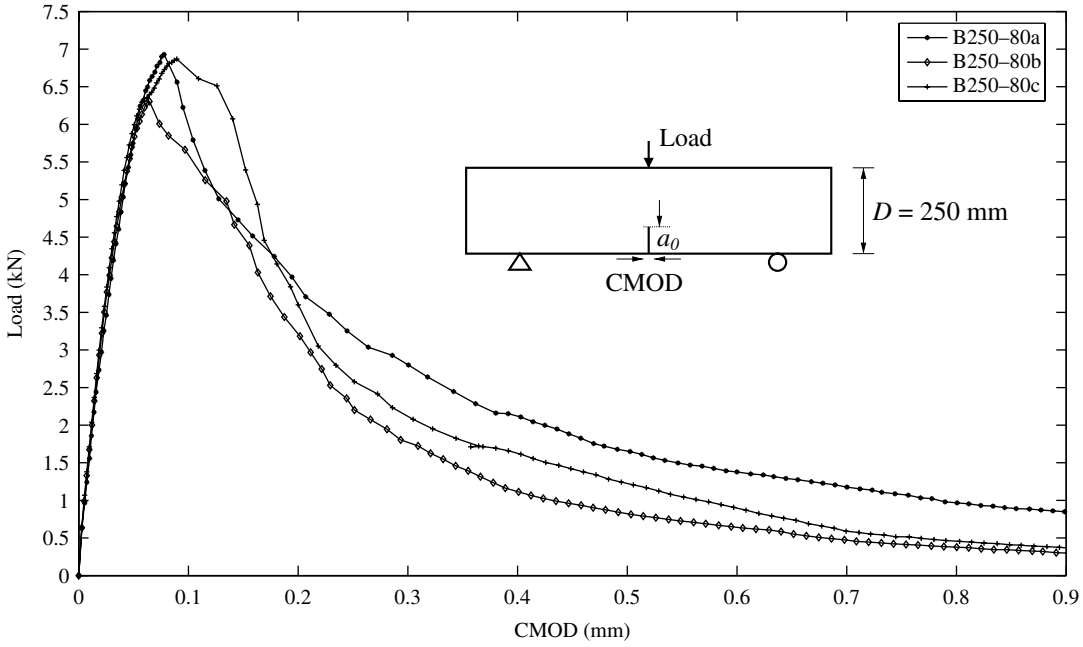

Fig. 7. Load–CMOD envelope curves for 250 mm depth specimens.

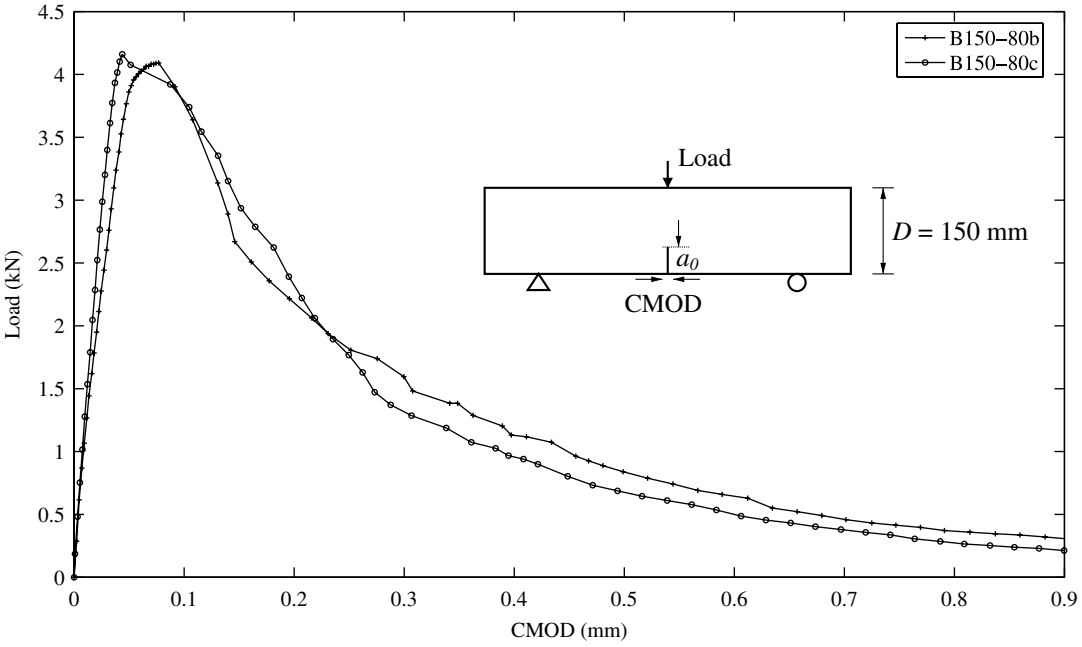

Fig. 8. Load–CMOD envelope curves for 150 mm depth specimens.

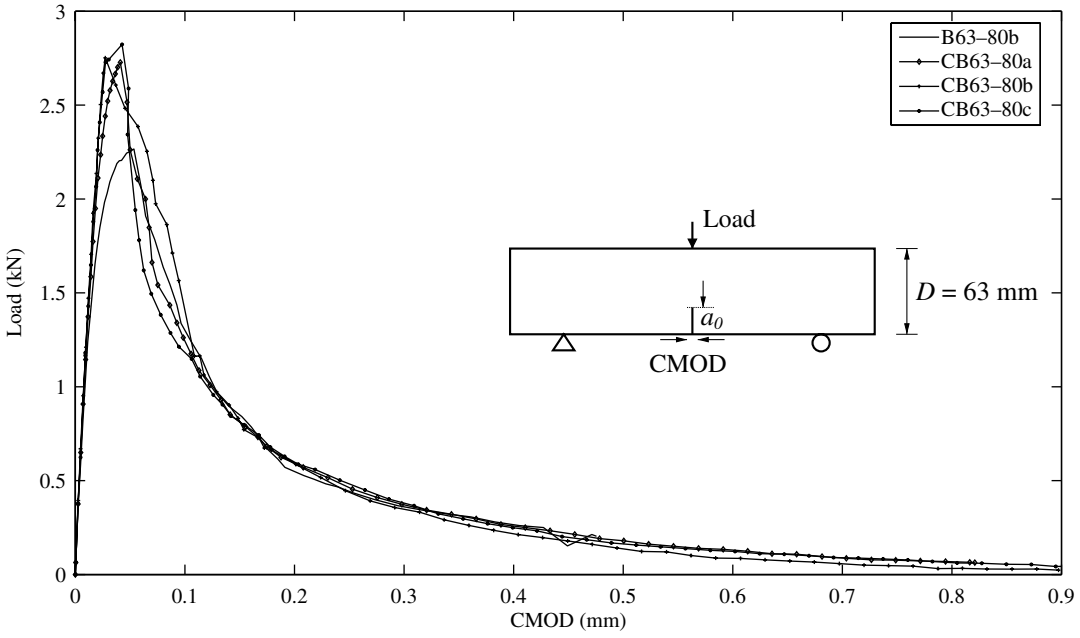

Fig. 9. Load–CMOD envelope curves for 63 mm depth specimens.

Table 5
Fracture parameters in the bilinear softening curve

	Specimen size (D) (mm)	Initial fracture energy (G_f) (N/m)		Tensile strength (f'_t) (MPa)	Total fracture energy (G_F) (N/m)	Stress change point (ψ)
		TPFM	SEM			
Fig. 10a	63	56.57	52.06	4.15	119	0.25
Fig. 10b	150	56.57	52.06	4.15	164	0.25
Fig. 10c	250	56.57	52.06	4.15	167	0.25

self-weight), P_w is the equivalent self weight force, and δ_0 is the CMOD displacement corresponding to $P_a = 0$ [28]. Because the specimen usually failed with $P_a > 0$, δ_0 was the CMOD at failure. The equivalent self weight force is calculated as $P_w = (S/2L)mg$, where S is the testing span, L is the length and mg is the mass (m) time gravity (g) weight of the beam. The total fracture energy was calculated as

$$G_F = \frac{W_t}{(D-a_0)t} = \frac{W_0 + 2P_w\delta_0}{(D-a_0)t}. \quad (8)$$

Table 4 shows the total fracture energy for each group of specimens. The averaged for the specimens with 250, 150, and 63 mm depth, was 167, 164, and 119 N/m, respectively. The total fracture energy remains constant for specimens with a depth of 250 and 150 mm, but decreases to 119 N/m for the depth of 63 mm. Figs. 7 and 8 show the variability of the peak load and area under the envelope curve for the 250 mm and 150 mm depth samples, respectively. Table 4 reports and its coefficients of variation for the 250, 150 and 63 mm specimens, respectively.

Fig. 9 compares the peak load and area under the envelope curve of the cast and saw-cut notch specimens. The saw-cut notch specimens had a very small coefficient of variation between specimens and a higher peak load than the cast notch specimen.

4.2. Critical stress intensity factor (K_{IC}) and critical crack tip opening displacement ($CTOD_C$)

Both K_{IC} and $CTOD_C$ were derived from Jenq and Shah's [29] effective elastic crack model called the two-parameter fracture model (TPFM). The equations and the complete procedure are presented in Appendix A.1. With this method, individual values of K_{IC} and $CTOD_C$ are obtained for each sample as seen in Table 4. The TPFM assumes the fracture properties are inherent material properties [21]. Therefore, K_{IC} and $CTOD_C$ for all specimen sizes were averaged which resulted in 1.13 MPa $m^{1/2}$ and 0.0180 mm with a coefficient of variation of 17% and 41%, respectively. As seen in Table 4, samples B150-80a and B63-80b have no results available (N/A), because the test data turned out to be erroneous. Sample B63-80c had all results except due to an operator error on the second load cycle.

4.3. Initial fracture energy (G_f) and characteristic fracture process zone length (c_f)

The initial fracture energy (G_f) and characteristic fracture process zone length (c_f), based on the size effect method [9,30,31] are also derived from an effective elastic crack assumption. The nominal strength (σ_N) of a structure is related to the specimen size (D) and the concrete fracture properties by the following equation:

$$\sigma_N = \frac{c_n K_{if}}{\sqrt{g'(\alpha_0)c_f + g(\alpha_0)D}}, \quad (9)$$

where c_n is the coefficient representing different types of structures, K_{if} is the stress intensity factor for an infinite

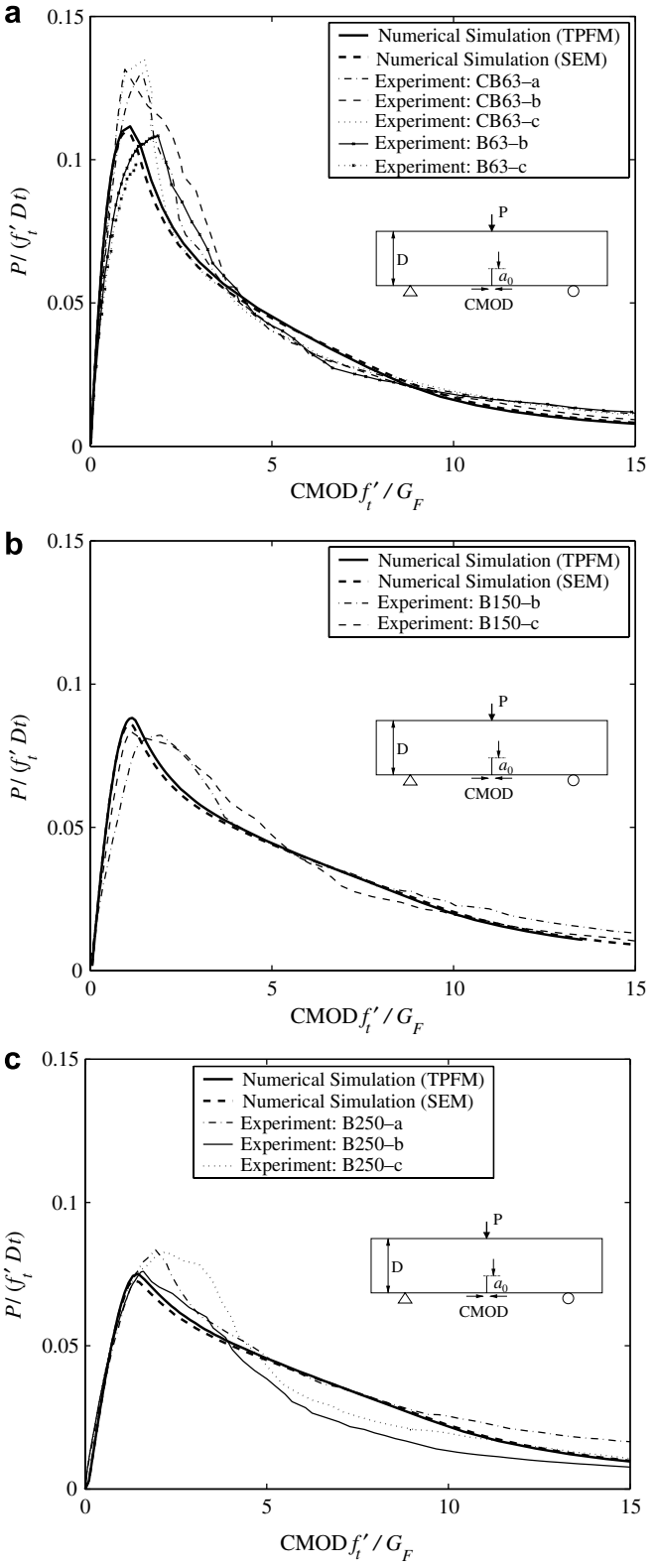

Fig. 10. Results of predicted load–CMOD curves compared with experimental data: (a) specimen size, $D = 63$ mm, (b) specimen size, $D = 150$ mm, and (c) specimen size, $D = 250$ mm.

specimen size and $g(\alpha)$ is a non-dimensional geometrical factor. For plane stress, the energy release rate is simply related to the stress intensity factor K_{if} and the modulus of elasticity E by

$$G_f = \frac{K_{if}^2}{E}. \quad (10)$$

Using the three geometrically similar specimens as seen in Table 4, a single set of fracture parameters, G_f and c_f, can be obtained from the peak load of each specimen and respective specimen self-weight. The SEM equations and the complete procedure are presented in Appendix A.2.

5. Simulation results

The experimental load–CMOD curves were predicted through numerical simulation of the CZM for each specimen size whose fracture parameters are provided in Table 5. The cohesive zone model was run with two separate initial fracture energies, one from the TPFM (56.6 N/m) and the other from the SEM (52.1 N/m). The average tensile strength (4.15 MPa) was assumed to be equal to the split tensile strength. The total fracture energy (average) for each specific specimen size was derived from Table 4. The stress ratio at the kink point (ψ) was assumed to be 0.25 based on work presented by Wittmann et al. [18]. In addition, the kink point can be determined as the stress ratio when the opening width equals the $CTOD_C$ [14]. In the numerical implementation, w_{cr} was calculated as a percentage (0.2%) of the final crack opening width (w_f). The critical crack opening width (w_{cr}) for all specimens was approximately 0.04 μm. These values of w_{cr} were found to be small enough to obtain the converged load–CMOD curves. Fig. 10 illustrates the correspondence between the numerical prediction and the experimental results for each specimen size. The determination of the softening curve in the numerical prediction was directly based on the experimental fracture properties obtained from the TPFM and SEM. No further steps were needed to fit the numerical simulations with the experimental results. These results are of key importance because they show that the load–CMOD curve for geometrically similar specimens can be predicted based upon fracture properties measured using standard tests.

The peak load of the experiment, which is essential to determine the concrete fracture properties, was compared to the peak load obtained from the numerical simulation. Although the peak load was under predicted for the 63 mm and 250 mm beam depth, the error was less than 10% as shown in Table 6. There was also little difference between the numerical simulation curves between the TPFM and SEM because of the small difference between their respective initial fracture energy values. The TPFM resulted in a slightly larger peak load due to its higher initial fracture energy. The total fracture energy of the experiment was also compared to that of the numerical simulation (Table 6). The calculated G_F from the numerical simulation, could not represent the complete separation of the specimens due to numerical instability at larger crack opening widths. Therefore, the simulated load–CMOD curves were extrapolated to the averaged CMOD at complete separation. Good agreement still exists between the G_F obtained from the experiments and numerical simulation. Furthermore, the friction at the support and the evaluation of the self-weight (Eq. (8)) would also result in some difference between the experimental and simulation results.

5.1. Model sensitivity

Other investigators have studied the sensitivity of the softening curve parameters on the numerical prediction of load–CMOD curves [32,33]. In this study, the sensitivity of the predicted load–CMOD curve for the three experimental fracture parameters (G_f, f_t' and G_F) and the stress ratio at the kink point (ψ) was also investigated to deter-

Table 6
Comparison of the peak load and the total fracture energy between experimental data and the numerical simulation

Specimen size (D) (mm)	Peak load (P_c)					Total fracture energy (G_F)		
	Experimental data – kN mean (range)	Numerical simulation (kN)		Error (%)		Experimental data – N/m (range)	Numerical simulation (N/m)	Error (%)
		TPFM	SEM	TPFM	SEM			
63	2.52 (2.05–2.82)	2.34	2.3	7.14	8.73	119 (106–124)	113	5.0
150	4.12 (4.09–4.16)	4.39	4.29	6.55	4.13	164 (159–170)	152	7.3
250	6.70 (6.31–6.93)	6.23	6.05	7.01	9.70	167 (139–193)	163	2.4

Table 7
Bilinear softening curve fracture parameters for sensitivity analysis

	Specimen size (D) (mm)	Initial fracture energy (G_f) (N/m)	Tensile strength (f_t') (MPa)	Total fracture energy (G_F) (N/m)	Stress change point (ψ)
Fig. 11a	150	56.57	4.15/5.83	164	0.25
Fig. 11b	63	56.57	4.15	119/167	0.25
Fig. 11c	63	56.57	4.15	119	0.15/0.25/0.33

mine if the trends would be consistency with past findings. These four fracture parameters in the bilinear softening curve are listed in Tables 5 and 7. As shown in Fig. 10, a larger initial fracture energy produced a greater normalized peak load ($P/f'_t tD$) at failure for a given f'_t, G_F and ψ. After the peak load, the two softening curves converged because both total fracture energies were identical. The numerical prediction of the measured tensile strength (4.15 MPa) was compared with an additional simulation where the tensile strength (5.83 MPa) was assumed to be the 10% of the measured compressive strength. Since the tensile strength is assumed to be the fracture initiation criterion, the peak load is greatly affected by changes in f'_t, as shown in Fig. 11a. With greater tensile strength materials for a fixed G_f, G_F and ψ, the slope of the load–CMOD curve become steeper, which corresponds to more brittle behavior.

In order to determine the sensitivity of the simulation to G_F, the total fracture energy of a 63 mm specimen (119 N/m) and that obtained from the 250 mm specimen (167 N/m) are used to predict the behavior of the 63 mm specimen in Fig. 11b. As the total fracture energy reduces for a fixed G_f, f'_t and ψ, only the post-peak behavior of the specimen is influenced but not the structure's peak load (related to the nominal strength). Finally, the sensitivity of ψ to the post-peak load behavior is examined through three different kink point stress ratios (0.15, 0.25, and 0.33) in Fig. 11c. The magnitude of the kink point stress does not affect the peak load but as the kink point stress ratio decreases from 0.33 to 0.15, the tail of the softening curve is extended. As expected, the initial fracture energy and the tensile strength are essential parameters to determine the strength of specimens while ψ and G_F influence the post-peak behavior.

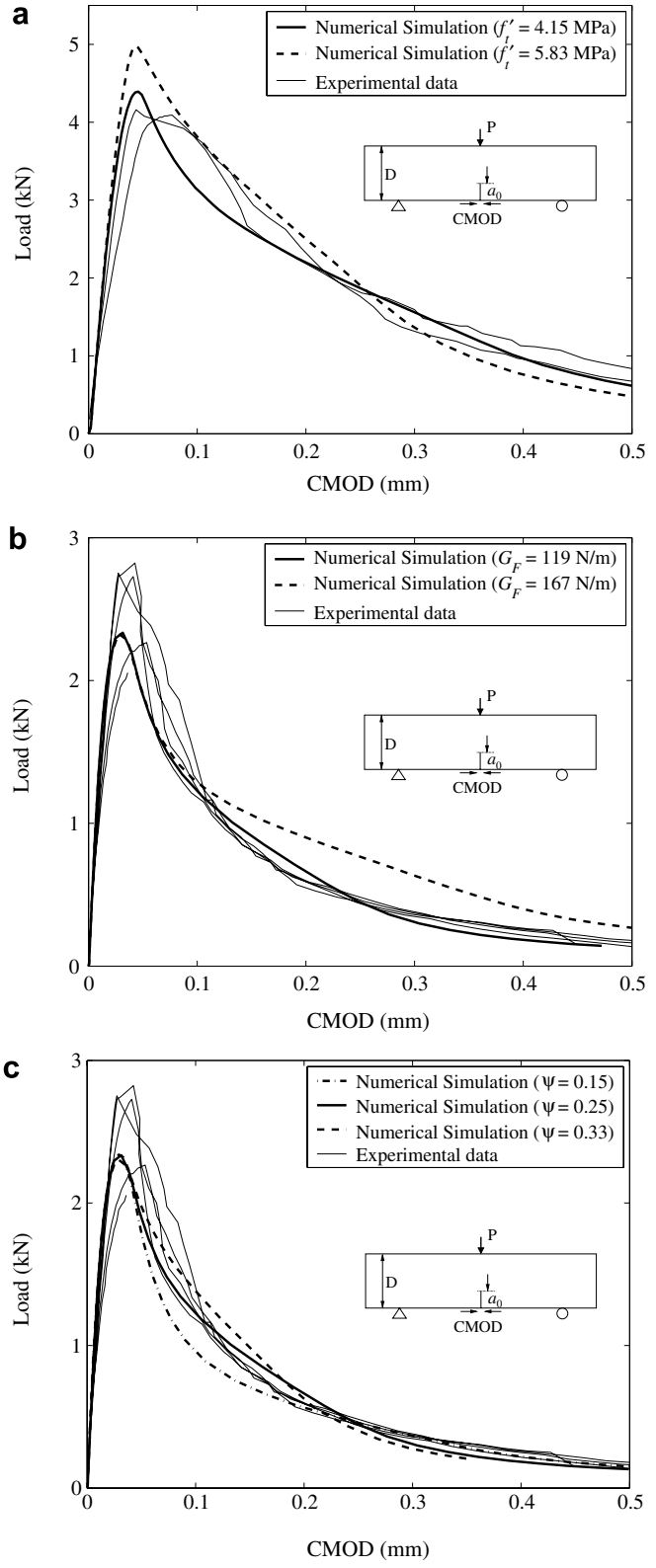

Fig. 11. Results of predicted load–CMOD curves compared with experimental data: (a) sensitivity of the tensile strength ($D = 150$ mm), (b) sensitivity of the total fracture energy ($D = 63$ mm), and (c) sensitivity of the ratio of the stress at the kink point ($D = 63$ mm).

5.2. Size effect

The nominal strength (σ_{Nu}) has been conveniently defined as the peak load divided by the beam depth and width [9]. It allows graphing specimens of different depths and peak loads on the same figure. The nominal strength is not necessarily equal to the flexural or beam strength of the concrete. The influence of the structural size (D) on the nominal strength (σ_{Nu}) was examined from the experiment and the numerical simulation results. Both experimental and numerical nominal strength are plotted in Fig. 12 with the size effect expression:

$$\sigma_{Nu} = \frac{Bf'_t}{\sqrt{1 + D/D_0}}, \tag{11}$$

where the non-dimensional constant, B, and the length dimensional constant, D_0, can be determined by the two experimental SEM parameters (G_f, c_f) [30]. Also, the two TPFM parameters (K_{IC}, $CTOD_C$) can be exploited to determine the constants (B, D_0) in the size effect expression by relating the $CTOD_C$ to the critical effective crack extension through the following equation [21]:

$$c_f = \frac{\pi}{32}\frac{CTOD_C^2 E}{G_f}. \tag{12}$$

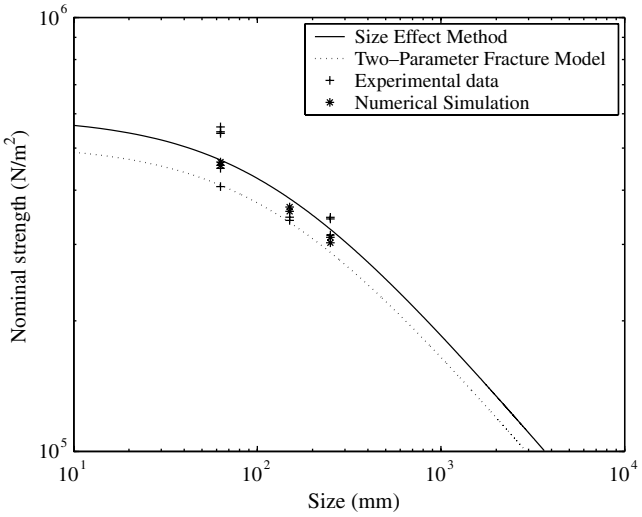

Fig. 12. Specimen size effect for three-point bend test configuration with notch depth ratio of 0.33.

The size effect model calculated from the SEM parameters closely resembles the model obtained from the TPFM parameters, as seen in Fig. 12. Furthermore, the nominal strength of both size effect models is similar to that of the experiment and the numerical simulation.

6. Conclusion

Physical experiments and finite element simulations based on the cohesive zone model for concrete were integrated to predict the monotonic fracture behavior of geometrically similar three-point bend specimens. A bilinear softening model was derived from measured fracture properties and implemented into a finite element-based cohesive zone model (CZM). In this CZM, cracking must propagate vertically along a predefined surface where cohesive elements have been inserted a priori. Three experimental fracture parameters (G_f, f'_t and G_F) defined the bilinear softening model. The initial fracture energy, the tensile strength and the stress ratio at the kink point were the material dependent fracture parameters, while the total fracture energy was dependent on the specimen size. The global behavior (load–CMOD) of the concrete specimens was captured by the numerical simulation. As expected, the initial fracture energy and the tensile strength are the significant controllers of the peak load of the specimen in the computational model, whereas the total fracture energy and the stress ratio at the kink point influence the post-peak load behavior of the specimen. Moreover, the experimental results and numerical simulation agree with the size effect expression whose constants can be determined by either the TPFM or the SEM.

Acknowledgements

This paper was prepared from a study conducted in the Center of Excellence for Airport Technology, funded by the Federal Aviation Administration under Research Grant Number 95-C-001 and the University of Illinois. The contents of this paper reflect the views of the authors, who are responsible for the facts and accuracy of the data presented within. The contents do not necessarily reflect the official views and policies of the Federal Aviation Administration. This paper does not constitute a standard, specification, or regulation.

Appendix A

A.1. TPFM calculation procedure

The TPFM requires at least one cycle to obtain the loading (C_i) and unloading (C_u) compliances, and also the peak load (P_c). The self-weight (P_0) of the specimen is also included. The critical effective elastic crack length (a_c) at the peak load is calculated from the modulus of elasticity obtained with the loading and unloading compliance, E_1 and E_2, respectively [28]:

$$E_1 = \frac{6Sa_0 g_2(\alpha_0)}{C_i D^2 t}, \tag{13}$$

$$E_2 = \frac{6Sa_c g_2(\alpha_c)}{C_u D^2 t} \tag{14}$$

with

$$\alpha_0 = \frac{(a_0 + \mathrm{HO})}{(D + \mathrm{HO})}, \tag{15}$$

$$\alpha_c = \frac{(a_c + \mathrm{HO})}{(D + \mathrm{HO})}, \tag{16}$$

$$g_2(\alpha) = 0.76 - 2.28\alpha + 3.87\alpha^2 - 2.04\alpha^3 + \frac{0.66}{(1-\alpha)^2}. \tag{17}$$

By equating E_1 and E_2, the critical effective elastic crack length a_c can be obtained.

Using the following LEFM relationship, K_{IC} and CTOD_C can be calculated given the geometric function (g_1) for the TPB specimen,

$$K_{IC} = 3(P_c + 0.5P_0 S/L)\frac{S\sqrt{\pi a_c} g_1(a_c/D)}{2D^2 t}, \tag{18}$$

where

$$g_1\left(\frac{a_c}{D}\right) = \frac{1.99 - (a_c/D)(1 - a_c/D)[2.15 - 3.93(a_c/D) + 2.70(a_c/D)^2]}{\sqrt{\pi}[1 + 2(a_c/D)][1 - (a_c/D)]^{3/2}}, \tag{19}$$

$$\mathrm{CTOD}_c = 6(P_c + 0.5P_0 S/L)\frac{Sa_c g_2(a_c/D)}{ED^2 t} \times \left[(1-\beta_0)^2 + \left[1.081 - 1.149\left(\frac{a_c}{D}\right)\right](\beta_0 - \beta_0^2)\right]^{1/2}, \tag{20}$$

where

$$g_2\left(\frac{a_c}{D}\right) = 0.76 - 2.28\left(\frac{a_c}{D}\right) + 3.87\left(\frac{a_c}{D}\right)^2 - 2.04\left(\frac{a_c}{D}\right)^3 + \frac{0.66}{(1 - \frac{a_c}{D})^2} \tag{21}$$

and

$$\beta_0 = \frac{a_c}{a_0}. \quad (22)$$

A.2. SEM calculation procedure

The corrected load (P_j^0) for sample j is calculated as [9,28]:

$$P_j^0 = P_j + \frac{2S_j - L_j}{2S_j} g m_j, \quad (23)$$

where P_j^0 is the corrected load, P_j is the bulk load applied by the testing equipment, m_j is the mass of the specimen, S_j is the span of the specimen, L_j is the length of the specimen, g is gravity (9.81 m/s^2) and j is the specimen number (1, 2, 3, …, n). After obtaining the corrected load, the following parameters were calculated for each sample:

$$Y_j = \left(\frac{D_j t}{P_j^0}\right)^2, \quad (24)$$

$$X_j = D_j. \quad (25)$$

Both parameters can be plotted and a linear regression equation can be derived:

$$Y = A_B X + C_B. \quad (26)$$

The next step is to calculate G_f and c_f from the slope and y-intercept of the linear regression:

$$G_f = \frac{g(\alpha_0)}{E A_B} \quad (27)$$

and

$$c_f = \frac{g(\alpha_0)}{g'(\alpha_0)}\left(\frac{C_B}{A_B}\right), \quad (28)$$

$$g(\alpha_0) = \left(\frac{S}{D}\right)^2 \pi \alpha_0 [1.5 g_1(\alpha_0)]^2, \quad (29)$$

$$\alpha_0 = \frac{a_0}{D} \quad (30)$$

where

$$g_1(\alpha_0) = \frac{1.99 - (\alpha_0)(1-\alpha_0)[2.15 - 3.93\alpha_0 + 2.70\alpha_0^2]}{\sqrt{\pi}[1+2\alpha_0][1-\alpha_0]^{3/2}}. \quad (31)$$

References

[1] Bazant ZP. Size effect. Int J Solid Struct 2000;37:69–80.

[2] Hillerborg A, Modeer M, Petersson PE. Analysis of crack formation and crack growth in concrete by means of fracture mechanics and finite elements. Cement Concrete Res 1976;6:773–82.

[3] Barenblatt GI. The formation of equilibrium cracks during brittle fracture: general ideas and hypotheses, axially symmetric cracks. Appl Math Mech 1959;23:622–36.

[4] Dugdale DS. Yielding of steel sheets containing slits. J Mech Phys Solids 1960;8:100–4.

[5] Modeer M. A fracture mechanics approach to failure analysis of concrete materials. Report No. TVBM-1001, Division of Building Materials. Lund Institute of Technology, Lund, Sweden; 1979.

[6] Petersson PE. Crack growth and development of fracture zone in plane concrete and similar materials. Report No. TVBM-1006, Division of Building Materials. Lund Institute of Technology, Lund, Sweden; 1981.

[7] Roelfestra PE, Wittmann FH. Numerical method to link strain softening with failure of concrete. In: Wittmann FH, editor. Fracture toughness and fracture energy of concrete. Elsevier Science Publishers; 1986. p. 163–75.

[8] Mulule SV, Dempsey JP. Stress-separation curves for saline ice using fictitious crack model. ASCE J Eng Mech 1997;8:870–7.

[9] Bazant ZP, Planas J. Fracture and size effect in concrete and other quasibrittle materials. Florida: CRC Press; 1998.

[10] Xu XP, Needleman A. Numerical simulations of fast crack growth in brittle solids. J Mech Phys Solids 1994;42:1397–434.

[11] Ruiz G, Ortiz M, Pandolfi A. Three-dimensional finite-element simulation of the dynamic Brazilian test on concrete cylinders. Int J Numer Meth Eng 2000;48:963–94.

[12] Elices M, Guinea GV, Planas GJ. The cohesive zone model: advantages, limitations and challenges. Eng Fract Mech 2002;69:137–63.

[13] Song SH, Paulino GH, Buttlar WG. Simulation of crack propagation in asphalt concrete using a cohesive zone model. ASCE J Eng Mech 2006;132:240–9.

[14] Park K, Paulino GH, Roesler JR. Determination of the kink point in the bilinear softening model for concrete [to be submitted for publication].

[15] Cho KZ, Kobayashi AS, Hawkins NM, Barker DB, Jeang FL. Fracture process zone of concrete cracks. ASCE J Eng Mech 1984;110:1174–84.

[16] Gopalaratnam VS, Shah SP. Softening response of plain concrete in direct tension. ACI J 1985;82:310–23.

[17] Gustafsson PJ, Hillerborg A. Improvements in concrete design achieved through application of fracture mechanics. In: Shah SP, editor. Application of fracture mechanics to cementitious composites. Dordrecht, The Netherlands; 1985. p. 639–80.

[18] Wittmann FH, Rokugo K, Bruhwiller E, Mihashi H, Simopnin P. Fracture energy and strain softening of concrete as determined by compact tension specimens. Mater Struct (RILEM) 1988;21:21–32.

[19] Guinea GV, Planas J, Elices M. A general bilinear fit for the softening curve of concrete. Mater Struct (RILEM) 1994;27:99–105.

[20] Bazant ZP. Concrete fracture models: testing and practice. Eng Fract Mech 2002;69:165–205.

[21] Bazant ZP. Choice of standard fracture test for concrete and its statistical evaluation. Int J Fract 2002;118:303–37.

[22] ABAQUS. Version 6.2, H.K.S. Pawtucket: Hibbitt, Karlsson & Sorensen; 2002.

[23] Camacho GT, Ortiz M. Computational modeling of impact damage in brittle materials. Int J Solid Struct 1996;33:2899–938.

[24] Park K. Concrete fracture mechanics and size effect using a specialized cohesive zone model, Master Thesis, University of Illinois at Urbana-Champaign; 2005.

[25] Song SH, Paulino GH, Buttlar WG. A bilinear cohesive zone model tailored for fracture of asphalt concrete considering viscoelastic bulk material. Eng Fract Mech 2006;73:2829–48.

[26] Planas J, Elices M, Guinea GV. Measurement of the fracture energy using three-point bend tests: Part 2 – influence of bulk energy dissipation. Mater Struct (RILEM) 1992;25:305–12.

[27] Hillerborg A. The theoretical basis of a method to determine the fracture energy GF of concrete. Mater Struct (RILEM) 1985;18:291–6.

[28] Shah SP, Swartz SE, Ouyang C. Fracture mechanics of concrete. New York: John Wiley & Sons; 1995.

[29] Jenq YS, Shah SP. Two parameter fracture model for concrete. J Eng Mech 1985;10:1227–41.

[30] Bazant ZP, Kazemi MT. Determination of fracture energy, process zone length and brittleness number from size effect, with application to rock and concrete. Int J Fract 1990;44:111–31.

[31] Issa MA, Issa MA, Islam MS, Chudnovsky A. Size effect in concrete fracture – Part II: analysis of test results. Int J Fract 2000;102:25–42.
[32] Roelfestra PE, Wittmann FH. Numerical method to link strain softening with failure of concrete. In: Wittmann FH, editor. Fracture toughness and fracture energy of concrete. Amsterdam: Elsevier Science Publishers; 1986.
[33] Elices M, Planas J. Fracture mechanics parameters of concrete: an overview. Adv Cement Based Mater 1996;4:116–27.